

Article

Characterizing and Monitoring Ground Settlement of Marine Reclamation Land of Xiamen New Airport, China with Sentinel-1 SAR Datasets

Xiaojie Liu ¹, Chaoying Zhao ^{1,2,3,*}, Qin Zhang ^{1,2,3}, Chengsheng Yang ^{1,2,3} and Jing Zhang ^{1,2,3}

¹ School of Geology Engineering and Geomatics, Chang'an University, Xi'an 710054, China; 2018026010@chd.edu.cn (X.L.); dczhangq@chd.edu.cn (Q.Z.); yangchengsheng@chd.edu.cn (C.Y.); racheljing@chd.edu.cn (J.Z.)

² National Administration of Surveying, Mapping and Geoinformation, Engineering Research Center of National Geographic Conditions Monitoring, Xi'an 710054, China

³ State Key Laboratory of Geo-Information Engineering, Xi'an 710054, China

* Correspondence: cyzhao@chd.edu.cn; Tel.: +86-29-8233-9251

Received: 10 February 2019; Accepted: 8 March 2019; Published: 11 March 2019



Abstract: Artificial lands or islands reclaimed from the sea due to their vast land spaces and air are suitable for the construction of airports, harbors, and industrial parks, which are convenient for human and cargo transportation. However, the settlement process of reclamation foundation is a problem of public concern, including soil consolidation and water recharge. Xiamen New Airport, one of the largest international airports in China, has been under construction on marine reclamation land for three years. At present, the airport has reached the second phase of construction, occupying 15.33 km². The project will last about twenty years. To investigate the temporal and spatial evolution of ground settlement associated with land reclamation, Sentinel-1 synthetic aperture radar (SAR) data, including intensity images and phase measurements, were considered. A total of 82 SAR images acquired by C-band Sentinel-1 satellite covering the time period from August 2015 to October 2018 were collected. First, the spatial evolution process of land reclamation was analyzed by exploring the time series of SAR image intensity maps. Then, the small baseline subset InSAR (SBAS-InSAR) technique was used to retrieve ground deformation information over the past three years for the first time since land reclamation. Results suggest that the reclaimed land experienced remarkable subsidence, especially after the second phase of land reclamation. Furthermore, 26 ground settlement areas (i.e., 0.015% of the whole area) associated with land reclamation were uncovered over an area of more than 1200 km² of the Xiamen coastal area from January 2017 to October 2018. This study offers important guidance for the next phase of land reclamation and the future construction of Xiamen New Airport.

Keywords: ground settlement; marine reclamation land; time series InSAR; Sentinel-1; Xiamen New Airport

1. Introduction

With the rapid development of modern cities, the efficiency of land-resource utilization has significantly risen. To alleviate pressure from dense populations, it is an important way to carry out marine reclamation land projects and expand urban space in coastal cities. Therefore, land reclamation activities have been performed in many countries around the world, including the USA [1], Singapore [2], the Netherlands [3], Japan [4], China [5], and other countries [6]. However, because land reclamation usually involves dumping uncompacted filling materials over unconsolidated marine sediments [7], the settlement process of reclamation foundation has become a problem of great public

concern. It can cause severe damage to structures such as harbors, highways, airport runways, and underground facilities. In addition, it greatly threatens the environment and public safety [8]. Therefore, it is necessary to characterize and monitor ground settlement associated with land reclamation to facilitate a better understanding of its temporal and spatial evolution. Accordingly, it can reduce economic loss and guarantee the safety of facility construction.

Traditionally, ground deformation could be quantitatively monitored by employing in-situ measurements such as GNSS, leveling, piezometers, and inclinometers. Although these methods have high accuracy, they still have maintenance problems and high costs due to discrete benchmark installation and campaign/continuous measurements [9]. More recently, repeat-pass spaceborne synthetic aperture radar interferometry (InSAR), which has been used in several regions, has proven to be a powerful geodetic tool for investigating ground settlement associated with land reclamation, with the advantages of wide spatial coverage, fine spatial resolution, and day-and-night and all-weather working capabilities. For instance, Jiang and Lin [10] investigated the long-term reclamation settlement of Hong Kong's Chek Lap Kok Airport by integrating InSAR and geological data; Yu et al. [11] applied COSMO-SkyMed and Sentinel-1 satellite images to investigate ground deformation in ocean-reclaimed areas of Shanghai, China; Liu et al. [12] determined surface deformation associated with land reclamation in Shenzhen, China from 2004 to 2010, and from 2013 to 2017, by combining the Envisat, COSMO-SkyMed, and Sentinel-1 datasets; Aslan et al. [13] investigated the spatial extent and rate of ground deformation related to land reclamation in the megacity of Istanbul, Turkey by using the ERS-1/2, Envisat, and Sentinel-1 datasets. These studies mainly focus on surface deformation investigation several years after the completion of land reclamation. Further, it would be great if the InSAR technique could be used for the real-time monitoring of ground deformation during the land reclamation process, because such a study could play an important decision-making role in the entire land reclamation process.

Compared with in situ measurements, the main concern of the InSAR technique lies in measuring precision. Theoretically, the measurement precision of InSAR largely depends on the coherence of interferograms, which is affected by many factors, including atmospheric artefacts, and temporal and spatial decorrelation [9,14]. Thanks to the successful launch of some new SAR satellites, e.g., TerraSAR-X, ALOS/PALSAR-2, and Sentinel-1, with the characteristics of short revisit period, short spatial baseline, and the provision of various wavelengths. For instance, the Sentinel-1 satellite flies in an orbital tube with a radius of 50 m, thus forming small orbit InSAR baselines in the order of 150 m [15], which significantly improves interferogram coherence and facilitates the improvement of InSAR measurement accuracy. Furthermore, advanced multitemporal InSAR (MT-InSAR) techniques could overcome many intrinsic temporal and spatial decorrelations of traditional InSAR techniques [16]. Currently, two main families of MT-InSAR techniques broadly exist, namely, the small baseline subsets (SBAS) [17–19] and persistent scatterers (PS) [20–22] methods. The former inverts surface deformation evolution through the singular-value decomposition (SVD) method using coherent interferograms.

Xiamen New Airport, as one of the most important international airports in China, four-fifths of which occupy an approximate area of 26 km², will be produced by marine reclamation land. Currently, the reclamation area has reached 10.58 km², and the construction of the airport will be finished in the next twenty years. Surface deformation occurs in land reclamation areas due to the soil consolidation of the underlying unconsolidated marine sediments [10]. However, there are no bibliographies available for ground deformation analysis on Xiamen New Airport. To bridge this gap, in this study, the SAR images of Sentinel-1 satellite were involved, and the time series InSAR method was employed to explore the spatiotemporal deformation characteristics of Xiamen New Airport after land reclamation. In addition, potential ground settlement areas associated with land reclamation in the coastal area of the city of Xiamen were also mapped and analyzed.

2. Study Area

Xiamen Xiang'an International Airport (Xiamen New Airport hereinafter) is located in the Xiang'an district, Xiamen, China [23], as shown in Figure 1, which is about 25 km to the west of the city center of Xiamen, and 15 km to the south of the county of Jinmen, Taiwan, China. The total planned area of the airport is about 31 km², as shown in the red line in Figure 2b, including the island of Xiaodeng, the shoal area between the islands of Dadeng and Xiaodeng, and part of the sea area around the island of Dadeng, as well as part of dry land in the east of Dadeng. Approximately 84% of the total airport area, occupying 26 km², will be created through the land reclamation project, which will be carried out in three phases: The first phase is mainly blowing and filling dredged mud, an area of about 3 km²; the second phase is mainly blowing and filling sands to create land, an area of about 7.58 km²; and the third phase is about 15 km², as shown in Figure 2a. At present, the first and the second phases of the project have been completed.

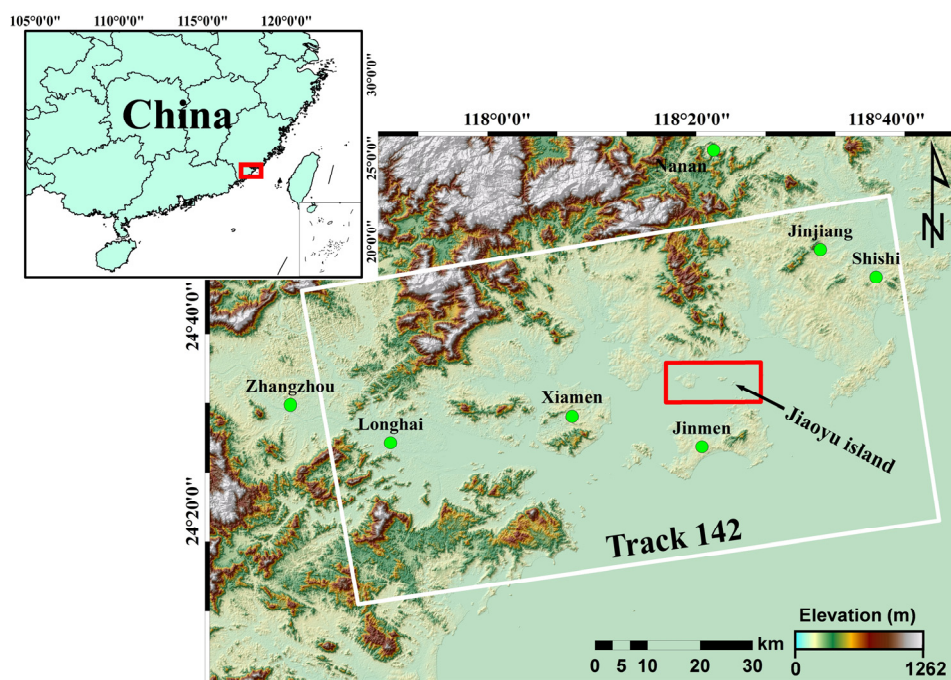


Figure 1. Study area location and synthetic aperture radar (SAR) data coverage. The background is the shaded topography generated from the shuttle radar topography mission digital elevation model (SRTM DEM), where the coverage of Sentinel-1 SAR data is superimposed by the white rectangle, green dots indicate the location of the major cities, and the red rectangle indicates the location of the study area. Inset indicates the study-area location in China.

The function area of the airport mainly includes the flight area, the terminal area, and the supporting area, and the runway is about 3800 m in length [23]. The engineering geology of Xiamen New Airport can be divided into five layers from top to bottom, that is, sand-mixed silt (Q_4^m) with a thickness of around 7.86 m, silt and silt mixed with sand (Q_4^s) with a thickness of around 7 m, silty clay and clay (Q_3^{al}) with a thickness of around 2.1 m, silty sand (Q_3^{sl}) with a thickness of around 4.9 m, and residual clay (Q^{el}) with a thickness of around 3.1 m. Two Landsat-8 remote sensing images of the airport were acquired on 26 March 2014 and 13 March 2018, which are shown in Figure 2a,b, respectively. It can be deduced that the airport did not start to reclaim until March 2014. However, the second phase of land reclamation was completed after March 2018.

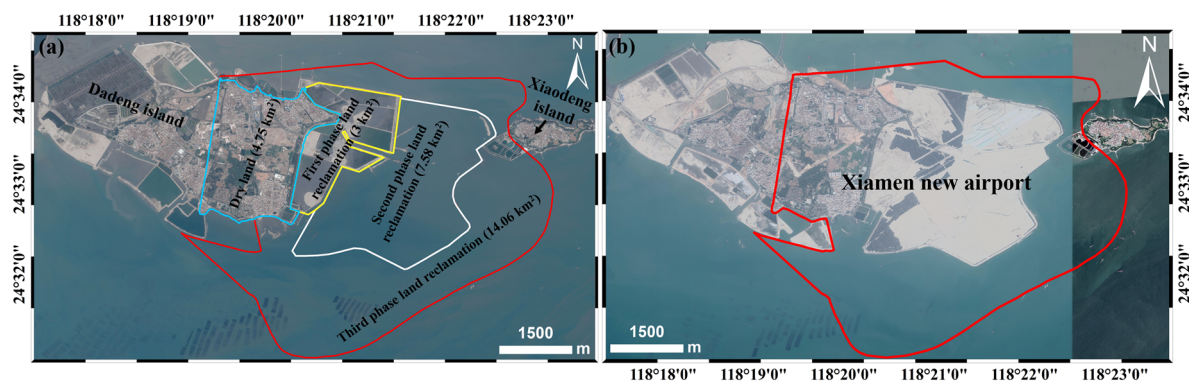


Figure 2. Landsat-8 remote-sensing images of the study area acquired on (a) 26 March 2014 and (b) 13 March 2018. The blue line represents the dry land area (4.75 km^2) of the airport, the yellow line indicates the first phase (3 km^2), the white line indicates the second phase (7.58 km^2), and the red line indicates the third phase (14.06 km^2) of marine reclamation land.

3. Data and Methodology

3.1. Datasets

A total of 82 ascending Sentinel-1 images acquired from 11 August 2015 to 24 September 2018 were employed to characterize and monitor the ground settlement of marine reclamation land. During the entire SAR data monitoring period, the land reclamation project was still underway, which caused the ground surface to greatly change. Therefore, in order to avoid the effect of SAR image decorrelation caused by ground surface changes, SAR data were divided into two groups for InSAR processing, that is, Group I, from November 2015 to December 2016, and Group II, from January 2017 to October 2018. The shuttle radar topography mission (SRTM) digital elevation model (DEM) with a resolution of 30 m was applied to remove topographic phase contributions. The topographic phase over Xiamen New Airport was negligible due to small elevation changes and the DEM missing during the land reclamation period. A multilooking factor of four in range direction was used in data processing, and the spatial resolution of multilooked SAR images was about 16 m in both range and azimuth directions. SAR images with this spatial resolution can best detect ground deformation.

GAMMA software was used to process the Sentinel-1 datasets [24]. The thresholds of the temporal baseline and the perpendicular baseline were set to 60 days and 150 m, respectively. Therefore, a total of 314 interferograms were generated and, eventually, 208 high-quality interferograms were selected to further calculate ground-surface deformation. The spatiotemporal baseline distributions of the high-quality interferograms are shown in Figure 3a,b, representing the interferograms in Group I and II, respectively.

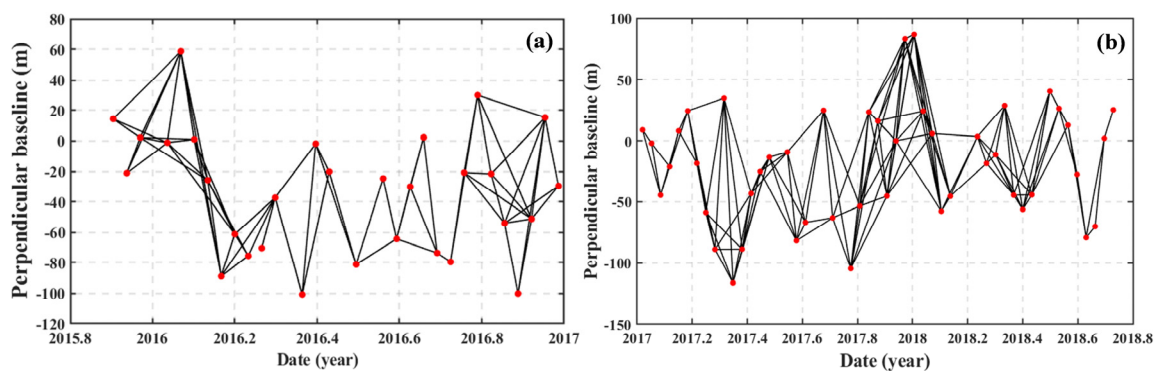


Figure 3. Baseline distribution of high-quality interferometric pairs used in this study. (a) Group I of SAR images, acquired from November 2015 to December 2016; (b) Group II of SAR images, acquired from January 2017 to October 2018.

3.2. Methodology

The temporal and spatial evolution of land changes and reclaimed land deformation of Xiamen New Airport were jointly investigated with the intensity and phase information of the SAR images.

First, Sentinel-1 images were preprocessed including coregistration, azimuth spectral filtering, image resampling, and data deramping and reramping [15]. With regard to the imaging mode of terrain observation by progressive scans (TOPS) for Sentinel-1 images, the Doppler Centroid rapidly varies along the track [15]. Phase ramps occur in individual bursts if coregistration accuracy is less than one-thousandth of one pixel, which is equivalent to 2 cm in azimuth [25]. Hence, highly precise coregistration, especially in the azimuth direction, is needed. Iterative coregistration refinement, estimated using intensity matching followed by the spectral diversity algorithm [26], was adopted for burst overlap areas to ensure that all SAR images were accurately coregistered.

As for analysis of the land reclamation process, intensity images were considered, which are robustly filtered with homogeneous pixels. First, statistically homogeneous pixels (SHPs) were selected using the fast SHP selection algorithm with the confidence interval for each pixel based on the central limit theorem [27]. Then, the intensity stacks were filtered by using the updated Lee filter algorithm [28] to remove speckle noise. It is worth noting that single-look intensity images and interferograms were used in this processing. As the accurate selection of SHPs is of great significance for the accurate estimation of intensity, SAR images were divided into four different time periods (i.e., from 11 August 2015 to 30 June 2016, from 24 July 2016 to 20 January 2017, from 1 February 2017 to 19 July 2017, and from 31 July 2017 to 24 September 2018) in order to avoid the influence of surface changes caused by land reclamation, and SHPs were estimated separately.

As for ground settlement monitoring, the differential interferograms were generated, filtered [29,30], and unwrapped [31,32] after the accurate coregistration of the SLC stacks. Baseline refinement was conducted to remove the residual orbital ramp phase [33]. The artifacts of atmospheric disturbance were reduced by using a quadratic polynomial model, as follows:

$$w(x, y) = a_0 + a_1x + a_2y + a_3xy + a_4x^2 + a_5y^2 \quad (1)$$

where $w(x, y)$ represents the unwrapped phase for a generic pixel (x, y) , a_i indicates the unknown coefficients, and i represents the subscript of the unknown coefficient a , corresponding to 1, 2, 3, 4, and 5.

As the study area is located in the coast, and the terrain is relatively flat, there is no need to consider the influence of the stratified atmospheric delay [34]. The average deformation rates and time series of the ground surface were calculated using Equation (2) [24] and the SBAS algorithm [17], respectively.

$$V_{phase} = \frac{\sum_{i=1}^N \Delta t_i \varphi_i}{\sum_{i=1}^N \Delta t_i^2} \quad (2)$$

where N is the number of interferograms, φ_i represents the unwrapped phase of each interferogram, and Δt_i is the time interval of each interferogram. Finally, the temporal and spatial deformation characteristics of ground settlement after land reclamation were analyzed in depth based on the deformation maps.

The ground deformation rate and time series obtained by Equation (2) and the SBAS algorithm are the sum of the projections of the real three-dimensional (i.e., north–south, east–west, and up–down) ground deformations in the line-of-sight (LOS) direction. For land subsidence caused by land reclamation, the vertical displacement dominates ground deformation [16]. Hence, to analyze the airport's deformation characteristics, the vertical deformations were mainly considered, and LOS displacement was purely back-projected into the vertical direction considering the local incidence angle [35].

4. InSAR Results

The surface deformation rate maps of Xiamen's coastal areas were retrieved from November 2015 to October 2018, as shown in Figure 4, where Figure 4a shows the one from November 2015 to December 2016, and Figure 4b from January 2017 to October 2018. Note that the deformation rate was in the LOS direction, and the positive values (blue color) indicate the motion toward the satellite (uplift), and the negative values (red color) indicate the motion away from the satellite (settlement). Figure 4 shows that most areas were stable (between -10 and 10 mm/year). However, several small-scale land deformation areas (<-10 mm/year) were obviously uncovered along the coastal areas of the city of Xiamen. Quantitatively, 20 land subsidence areas were detected from November 2015 to December 2016, and 26 land subsidence areas were detected from January 2017 to October 2018. The maximum annual subsidence rate from November 2015 to December 2016, and from January 2017 to October 2018 reached -130 mm/year and -126 mm/year, respectively.

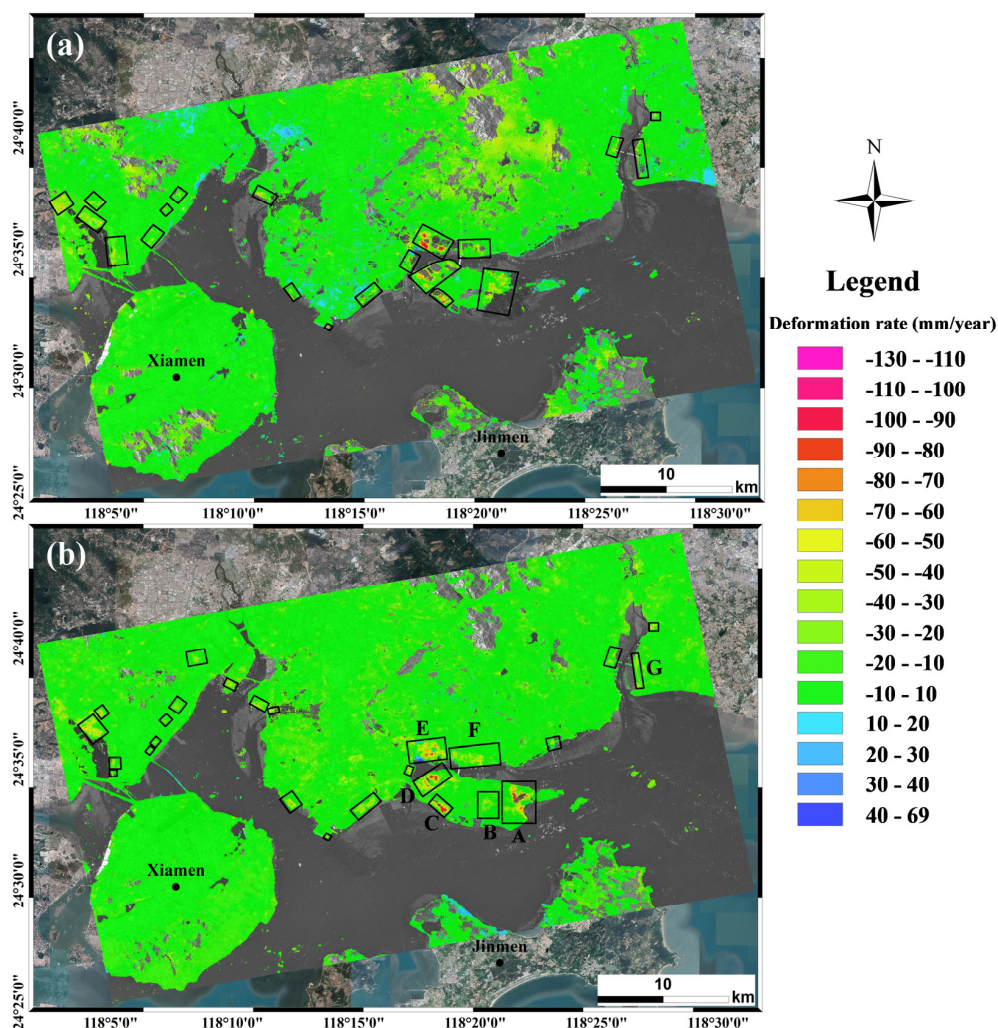


Figure 4. Average deformation rate maps calculated with Sentinel-1 datasets over the whole coastal areas of the city of Xiamen. Black rectangles represent potential deformation areas identified by InSAR, and Regions A–G in Figure 4b are analyzed in Section 5. (a) The deformation rate map from November 2015 to December 2016; (b) the one from January 2017 to October 2018.

It can also be seen from Figure 4 that moderate (between -30 and -40 mm/year) to strong (<-40 mm/year) land subsidence areas were mainly concentrated in the central coastal areas, i.e., the Xiang'an district of Xiamen. There was only one strong land subsidence area observed from November 2015 to December 2016, with the maximum deformation rate of -130 mm/year. However, it increased

to four regions (as shown in Regions A, C, D, and E in Figure 4b) from January 2017 to October 2018, which will be discussed in Section 5. In addition, some slight to moderate subsidence areas were also observed in the eastern (i.e., the eastern part of the Xiang'an district) and western (i.e., Jimei district) coastal areas of Xiamen, which were continuously deformed from November 2015 to October 2018, with the deformation rate ranging from -10 to -30 mm/year.

5. Analysis and Discussion

5.1. Spatial Evolution of Land Reclamation at Xiamen New Airport

Time series SAR intensity images of the Sentinel-1 over Xiamen New Airport from August 2015 to October 2016 were obtained, where four main land reclamation stages could be roughly reflected, as shown in Figure 5a,c,e,g. Four optical remote sensing images with similar acquisition dates are shown in Figure 5b,d,f,h. It can be seen from Figure 5 that the spatial evolution of land reclamation was clearly recorded in the SAR intensity maps including the following four stages, which could be well validated by the optical remote sensing images.

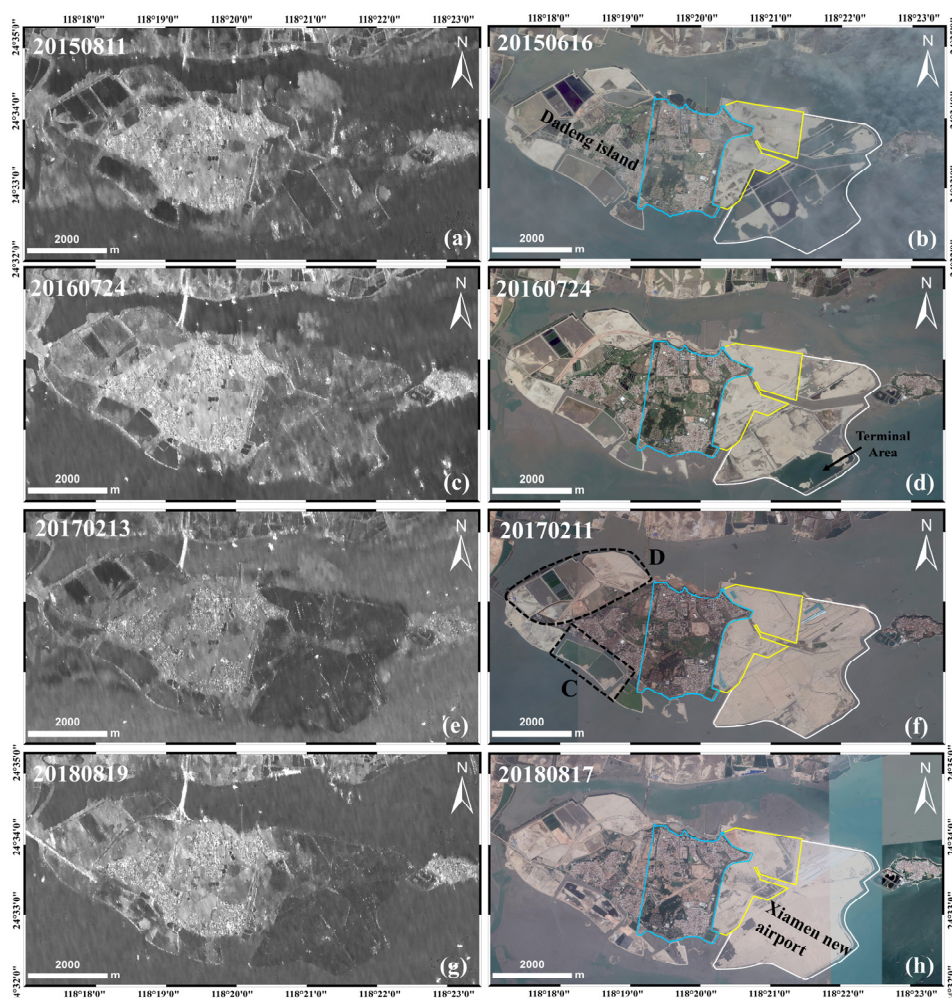


Figure 5. Four SAR intensity images and four remote sensing images of Xiamen New Airport. Intensity images were acquired on (a) 11 August 2015, (c) 24 July 2016, (e) 13 February 2017, and (g) 19 August 2018, respectively; remote sensing images were acquired on (b) 16 June 2015, (d) 24 July 2016, (f) 11 February 2017, and (h) 17 August 2018, respectively. Solid blue line represents the pre-existing land area of Xiamen New Airport, solid yellow line indicates the area of the first phase of land reclamation, and solid white line indicates the one in the second phase.

(1) The first phase of land reclamation, as shown with the yellow lines in Figure 5, was completed before 16 June 2015 (see Figure 5a,b); (2) except for the southeastern corner of the airport, i.e., the terminal area, other areas of the second phase of land reclamation were reclaimed before 24 July 2016 (see Figure 5c,d); (3) the second stage of land reclamation was fully completed on 13 February 2017, as shown with white lines in Figure 5e,f. However, the operation of soil compaction was not carried out, so water seepage can still be observed in local areas, e.g., in the central and southeastern parts of the airport (see Figure 5e,f); (4) the whole land reclamation area of the second phase was compacted on 19 August 2018 (see Figure 5g,h).

In addition, it can be seen from Figure 5 that the land reclamation project was conducted in Region C on 16 June 2015 (see Figure 5a,b) but was subsequently covered by seawater (see Figure 5c,d,e,f), and land reclamation was restarted on 19 August 2018 (see Figure 5g,h). For Region D, it is evident that land reclamation began on 24 July 2016 (see Figure 5a–d). By 19 August 2018, except for a small part of the central section, the land reclamation project in other areas was basically completed (see Figure 5g,h). However, water seepage could also be observed in the northeastern part of the region (see Figure 5g,h).

5.2. Spatiotemporal Deformation Patterns of Xiamen New Airport

To reveal the deformation characteristics and patterns of Xiamen New Airport after land reclamation, the deformation rate from January 2017 to October 2018 was enlarged in Figure 8a. Two remote sensing images, acquired on 22 January 2017 and 13 March 2018, were segmented into three sections to aid ground settlement analysis, as shown in Figure 8b,b',c,c',d,d'. It can be seen from Figure 8 that the pre-existing land is quite stable. However, four obvious subsidence areas associated with land reclamation could be successfully detected, two of which are located in the area of the first and second phases of the airport's land reclamation (i.e., Regions A and B), and the other two are located in the western and southwestern parts of the island of Dadeng (i.e., Regions C and D). Severe land subsidence occurred at Regions A, C, and D from January 2017 to October 2018, and the maximum deformation rate reached -126 mm/year in the LOS direction, while moderate land subsidence was observed in Region B, with a maximum deformation rate of around -48 mm/year. As mentioned in Section 5.1, the land reclamation date of Region B is much earlier than those of the other three regions, which indicates that the severe land subsidence occurred over newly reclaimed areas. An unusual phenomenon was observed in the terminal area (see Figure 5d), which showed to be quite stable even it was reclaimed at the latest date, which may be correlated with the reclamation methods and materials in the later stage. A similar phenomenon was observed in Chek Lap Kok Airport, Hong Kong [10].

Figure 6 shows the six cross-sections of vertical deformation rates in different areas to quantitatively analyze the correlation between the reclamation phases and ground surface settlement, where different colors indicate the different times of completed land reclamation. Ground settlement funnels can be clearly observed in all six profiles. However, the deformation patterns of settlement funnels in different reclamation areas show inconsistencies, i.e., the magnitudes of deformation vary in different areas. On the basis of Section 5.1 and Figure 6, it is evident that settlement funnels along the profiles of AA' and DD' experienced the largest deformation (< -130 mm/year; see Figure 6a,d), where the land reclamation project was completed on 13 February 2017. Deformation rates in the vertical direction were over -140 mm/year from January 2017 to October 2018. The settlement funnels along the profiles of CC', EE', and FF' experienced moderately large deformation (between -130 and -100 mm/year; see Figure 6c,e,f), deformation rates in the vertical direction were -111 , -125 , and -124 mm/year, respectively. It can be seen from Figures 5 and 8 that land reclamation of the maximum deformation area along profile CC' was completed on 13 February 2017. The settlement funnel along profile EE' was reclaimed on 16 June 2015 (see Figure 5b), but it was subsequently covered by seawater (see Figure 5d,f), and the land reclamation project was conducted again on 17 August 2018 (see Figure 5h). The settlement funnel along profile FF' was reclaimed on 24 July 2016, and water seepage

could still be observed on 17 August 2018. The settlement funnel along the profile BB' experienced relatively less deformation (> -100 mm/year) compared to former profiles, where land reclamation projects were completed on 15 June 2015, with a deformation rate as large as -93 mm/year in the vertical direction. Therefore, it can be concluded that the magnitude of ground deformation after land reclamation at Xiamen New Airport is closely correlated to the completion time of land reclamation projects, i.e., significant deformation occurred in newly reclaimed areas, and the deformation rate decreased as time went by. Such a deformation pattern is in good agreement with that of other land reclamation areas, such as Lingang New City in Shanghai, China [7]. In addition, the results reveal that most areas (e.g., Region A in Figure 8a) of the second phase of land reclamation are in a state of severe deformation, with the deformation rate in the vertical direction greater than -93 mm/year from January 2017 to October 2018.

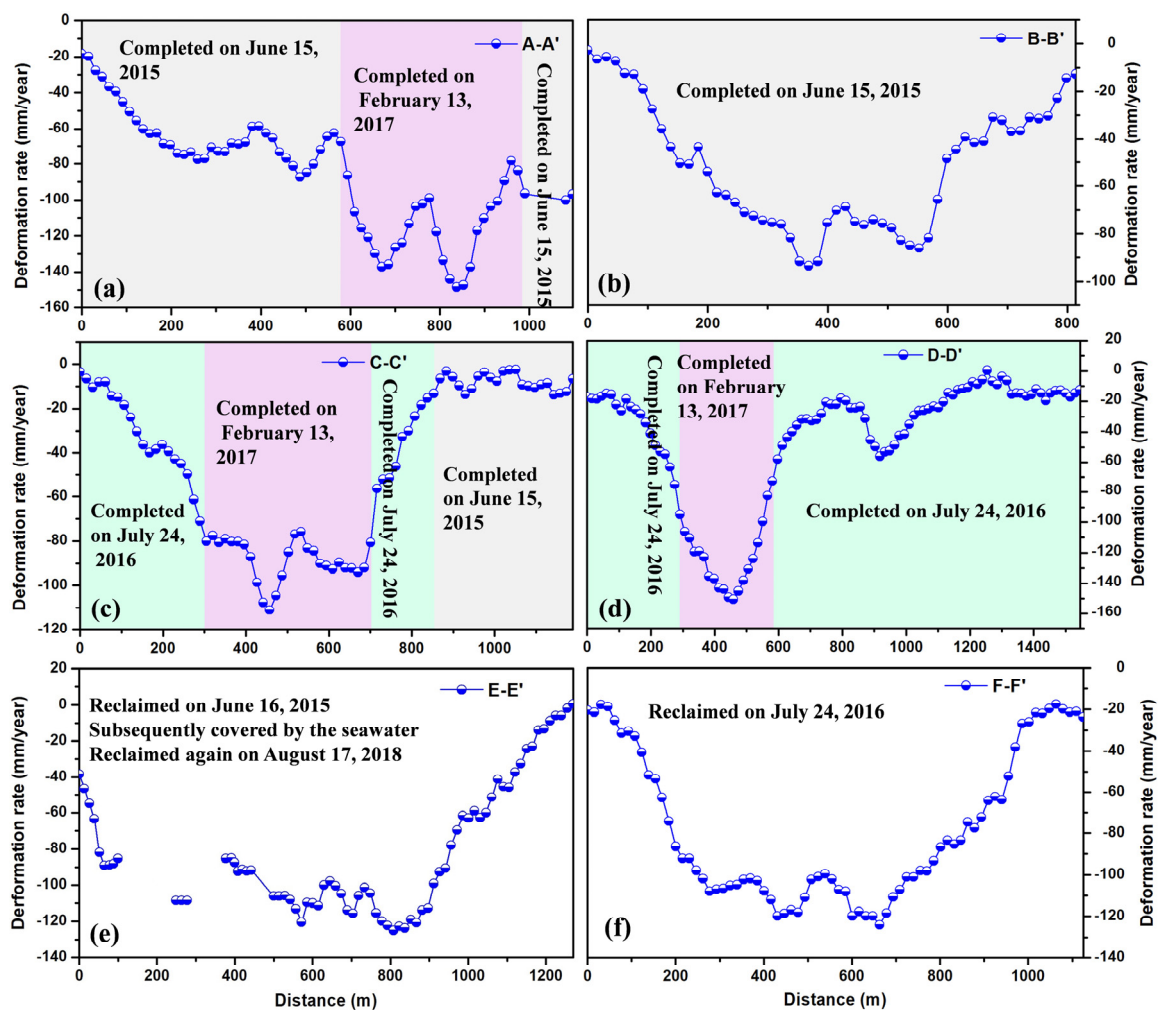


Figure 6. Cross-sections of average vertical deformation rates of Xiamen New Airport from January 2017 to October 2018 along six profiles, whose positions are marked in Figure 8. (a) Profile A–A'; (b) profile B–B'; (c) profile C–C'; (d) profile D–D'; (e) profile E–E'; (f) profile F–F'.

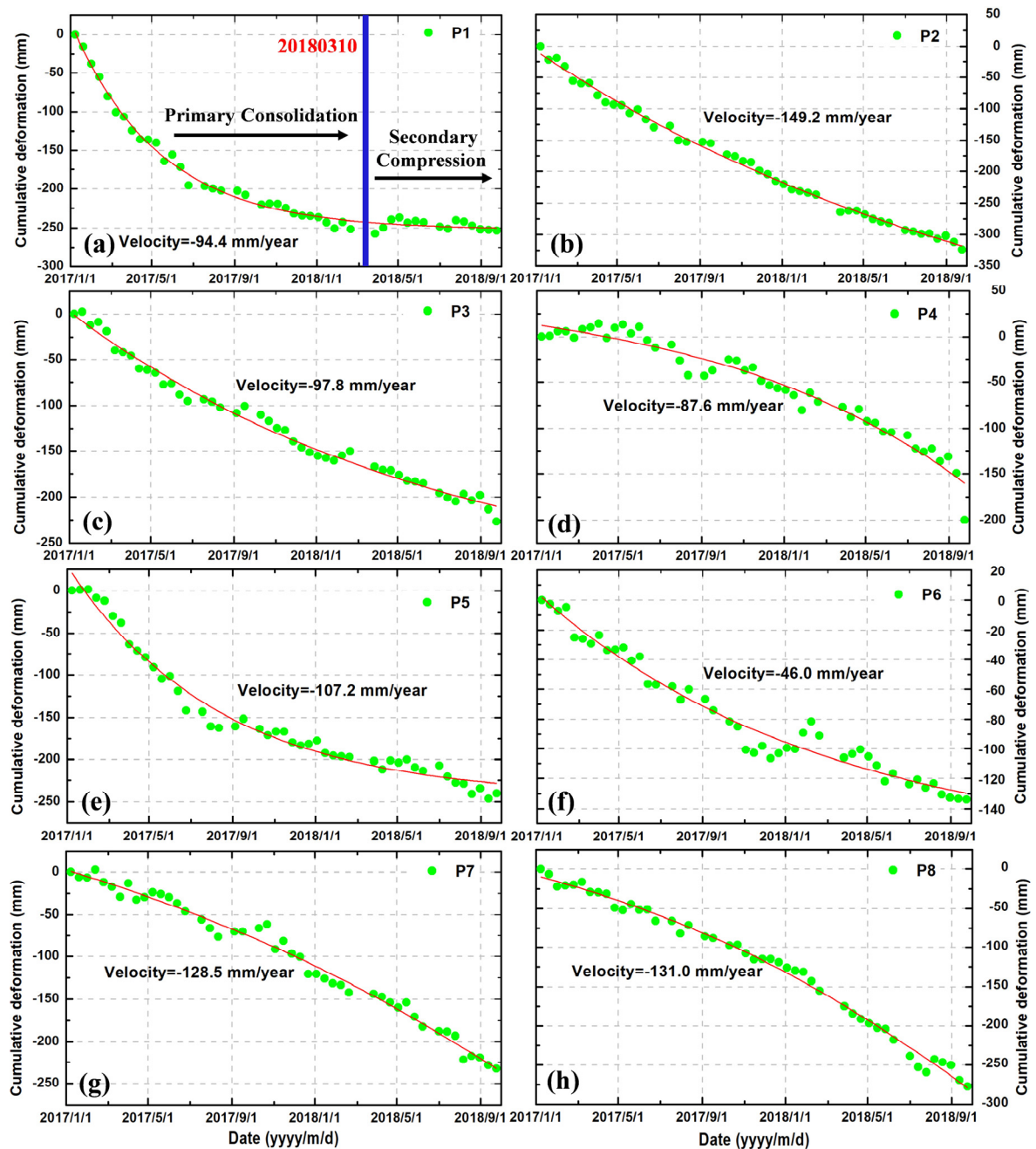


Figure 7. Time series deformation in the vertical direction of Xiamen New Airport from January 2017 to October 2018 for points P1 to P8. The locations of points P1 to P8 are shown in Figure 8. (a) Point P1; (b) point P2; (c) point P3; (d) point P4; (e) point P5; (f) point P6; (g) point P7; (h) point P8.

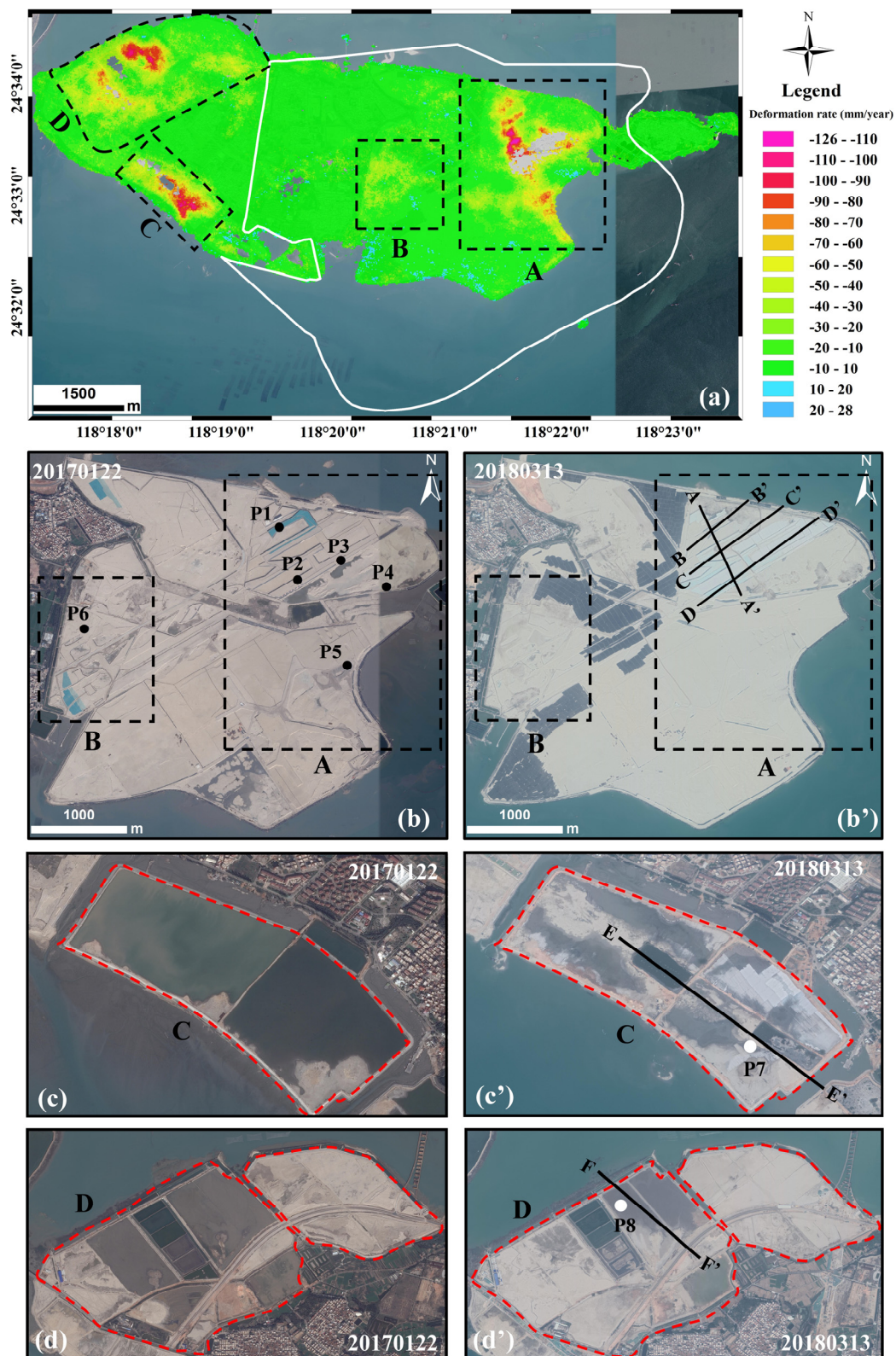


Figure 8. Ground deformation rate map (a) and three sections of remote sensing images acquired on 22 January 2017 in regions A, B, C, and D in (b), (c), and (d), respectively, and on 13 March 2018 in (b'), (c'), and (d'), respectively. Solid black lines from AA' to FF' denote profile locations, which are further shown in Figure 6. Points P1 to P8 (marked with black and white dots) are chosen to show the time series deformation in Figure 7.

To evaluate temporal deformation evolution after land reclamation at Xiamen New Airport, eight typical points, P1 to P8, located in different areas, were selected to analyze time series deformation with respect to the time table of land reclamation. The locations of the selected points are shown in Figure 8. P1 to P5 are located in Region A during the second land reclamation phase, P6 is in Region B during the first land reclamation phase, and P7 and P8 are in Regions C and D, as shown in Figure 8. From Figures 5 and 8, it can be seen that P6 was at the earliest completed reclamation region, and P2, P3, P7, and P8 were at the latest ones.

Figure 7 shows the time series vertical deformation of eight points from January 2017 to October 2018. It is evident that the eight points experienced nonlinear subsidence with various velocities. Maximum and minimum cumulative deformations were observed at P2 and P6, with a magnitude of -323 and -134 mm, respectively. In addition, large cumulative deformations were observed at P1 and P8, exceeding -250 mm in less than two years. The magnitude of the accumulated settlement also showed strong correlation with the time table of land reclamation. Furthermore, the eight points had different deformation evolutions. The subsidence trend at P1 slowed down in November 2017 and then turned into a relatively mild subsidence pattern, which suggested that the reclaimed land entered a long-term slow compression phase [7]. However, subsidence at P4, P7, and P8 still showed a large subsidence trend, which indicated that the newly reclaimed land had just been completed and would enter the phase of primary consolidation [10]. Accordingly, it is highly possible that P4, P7, and P8 could still undergo remarkable subsidence in the near future. Therefore, fieldwork should be done to further monitor the dense time series ground settlement. The detailed analysis of deformation evolution after land reclamation at Xiamen New Airport is provided in Section 5.5 based on Terzaghi theory of soil mechanisms [36].

5.3. Coastal Land Subsidence and Uplift

According to the InSAR measurements in Figure 4, there is remarkable subsidence associated with land reclamation that could be observed in most coastal areas of Xiamen, especially in Regions E and F. Detailed deformation rate maps for Regions E and F are shown in Figure 9, where Figure 9c shows the deformation rate from November 2015 to December 2016, and Figure 9d shows the deformation rate from January 2017 to October 2018. In addition, two remote sensing images acquired on 22 July 2016 and 13 March 2018, are shown in Figure 9a,b to facilitate deformation analysis. To reveal the spatial characteristics of land subsidence, three profiles located in different areas were selected to extract the deformation rates; profile locations are shown in Figure 9b, and deformation rates along the profiles are shown in Figure 10. Furthermore, the time series deformation for the four points shown in Figure 9b was obtained to further analyze the temporal evolution of land subsidence, as shown in Figure 11.

It can be seen from Figure 9a,b that Regions E and F were reclaimed on 22 July 2016 and were basically completed on 13 March 2018. However, obvious water seepage can still currently be observed in the reclamation areas, which indicates that the reclamation area is still in an unstable state. We can see from Figure 9c that the reclaimed areas for Regions E and F, from November 2015 to December 2016, suffered very large deformation. The deformation rate in the LOS direction reached -130 mm/year. From Figure 9d, we can see that the spatial deformation characteristics of Regions E and F changed after 2017. The magnitude of deformation slightly dropped, and results demonstrate that land subsidence gradually slowed down with the passing of time after land reclamation. However, the area of deformation greatly increased. The area of deformation between November 2015 and December 2016 was about 1.8 km², and it increased to 5.1 km² from January 2017 to October 2018. Obvious nonuniform land subsidence can be observed in Regions E and F in Figure 10, which is particularly evident in the location of Profile GG'. Such a nonuniform subsidence pattern could largely be attributed to the different completion times of land reclamation in different areas. Some obvious land subsidence funnels were detected at the locations of profiles HH' and II', and deformation rates in the vertical direction reached -105 and -61 mm/year from January 2017 to October 2018, respectively.

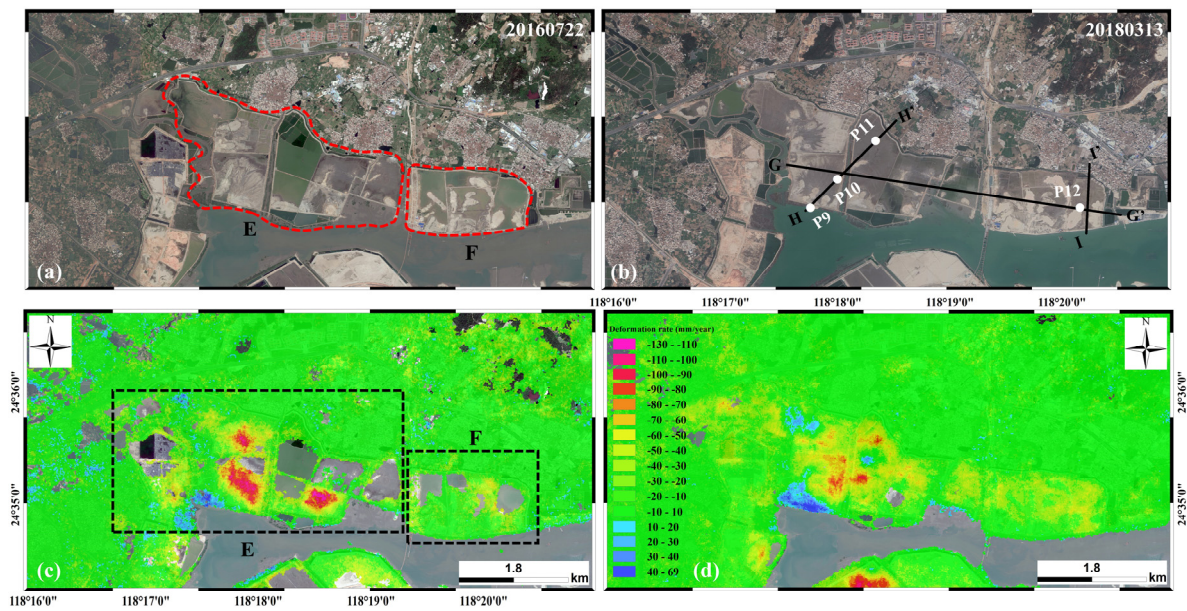


Figure 9. Ground deformation rate maps and remote sensing images of Regions E and F. (a) Remote sensing image acquired on 22 July 2016; (b) remote sensing image acquired on 13 March 2018; (c) average ground deformation rate map from November 2015 to December 2016; (d) average ground deformation rate map from January 2017 to October 2018.

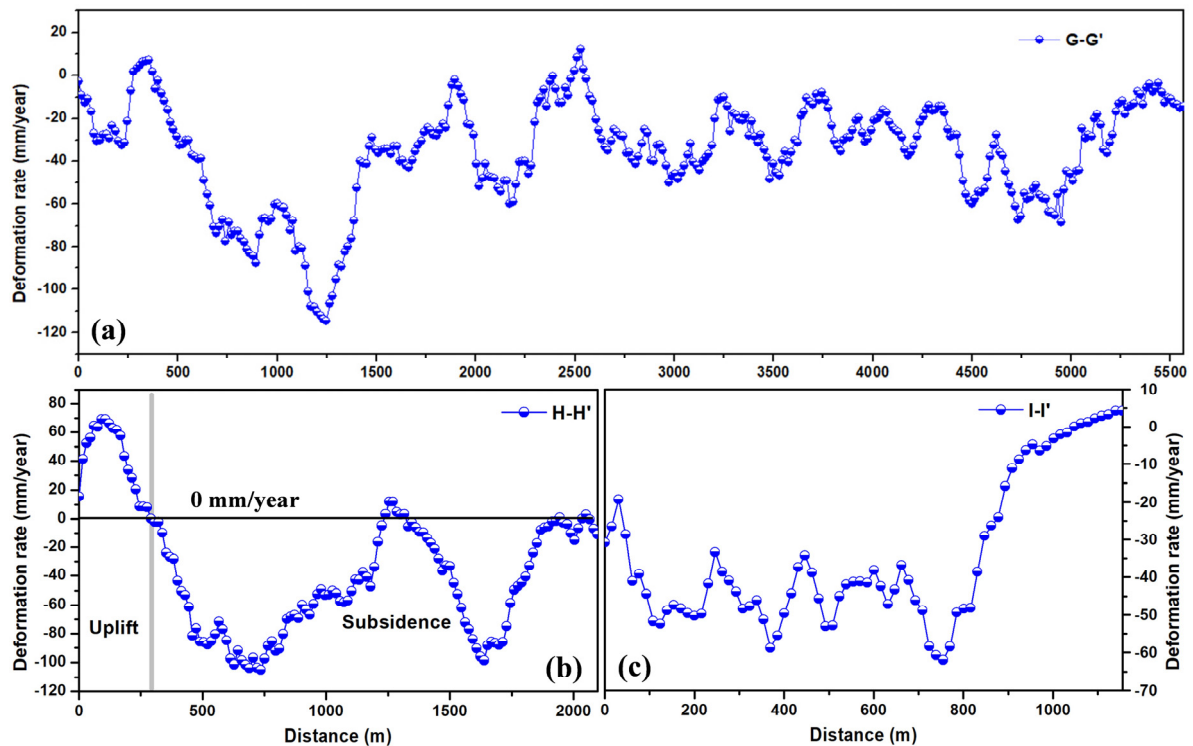


Figure 10. Average deformation rates in the vertical direction of Region E and F from January 2017 to October 2018 along three profiles (positions are indicated as black solid lines in Figure 9b). (a) Profile G–G'; (b) profile H–H'; (c) profile I–I'.

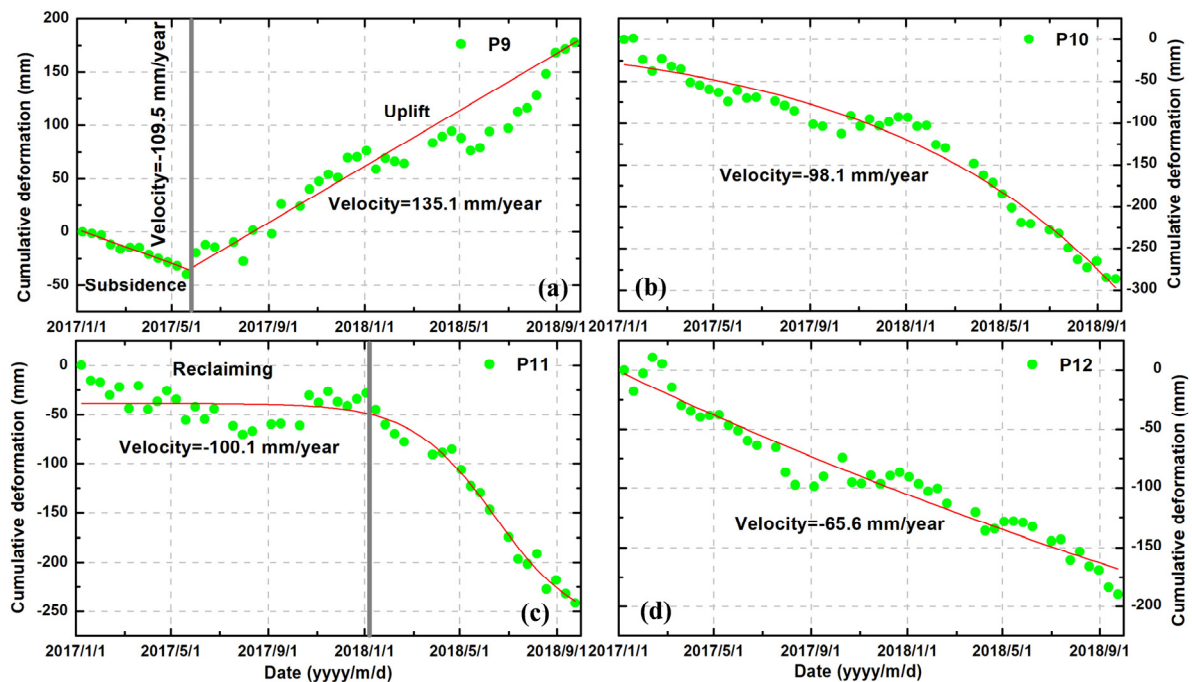


Figure 11. Time series deformation in the vertical direction of Regions E and F from January 2017 to October 2018 for P9–P12, which are indicated as white dots in Figure 9b. (a) Point P9; (b) point P10; (c) point P11; (d) point P12.

Different temporal evolution characteristics of deformation can be seen from Figure 11. It is clear that P10 and P12 suffered nonlinear subsidence from January 2017 to October 2018, while P11 had a different temporal deformation pattern. P11 deformation fluctuated before January 2018, then changed to rapid deformation until October 2018, which indicated that P11 was in the reclamation stage before January 2018 and began to deform after reclamation was completed in January 2018. These deformation patterns are in good agreement with the prediction pattern of unsaturated soil consolidation theory [37].

Besides land subsidence, several areas in Region E experienced remarkable uplift. P9 in Figure 11a was in the subsidence stage before August 2017, afterward turning to uplift. Such a phenomenon was also observed in other land reclamation cases [7], which can be explained by the well-known compression mechanisms of hydraulic fill. Generally, ground deformation associated with land reclamation is induced by primary consolidation and long-term second compression of alluvial clay deposits beneath the reclamation [10,16]. For newly reclaimed areas, such as P11, primary consolidation takes place for some time. Then, it moves on to the second stage, which is a slight rebound after long-term compression, such as in P9. Finally, land subsidence is in a stable state after long-term changes, such as in P1 [7]. Therefore, we can infer that the P9 uplift was caused by the rebound of reclamation fill materials after long-term compression.

5.4. Subsidence Along the Road

In addition to deformation caused by extensive land reclamation, typical deformation caused by road construction was also observed in the northeastern part of Xiamen, as shown in Region G in Figure 4b. Figure 12 shows the ground deformation rate of Region G from January 2017 to October 2018, and two remote sensing images acquired on 6 February 2015 and 18 May 2018. It is evident from Figure 12a that the road in the northern section was constructed before 6 February 2015, while the remaining sections were basically completed before 18 May 2018 (Figure 12c). It can be seen from Figure 12b that there was obvious deformation that occurred on the road built in the later stage, which did suffer slow-rate subsidence, with the deformation rate in the LOS direction of about -20 to

−40 mm/year from January 2017 to October 2018. No deformation could be observed for the road built in earlier years, which can be explained because the earlier built road was completely compacted, whereas the newly built one is still under the compaction process.

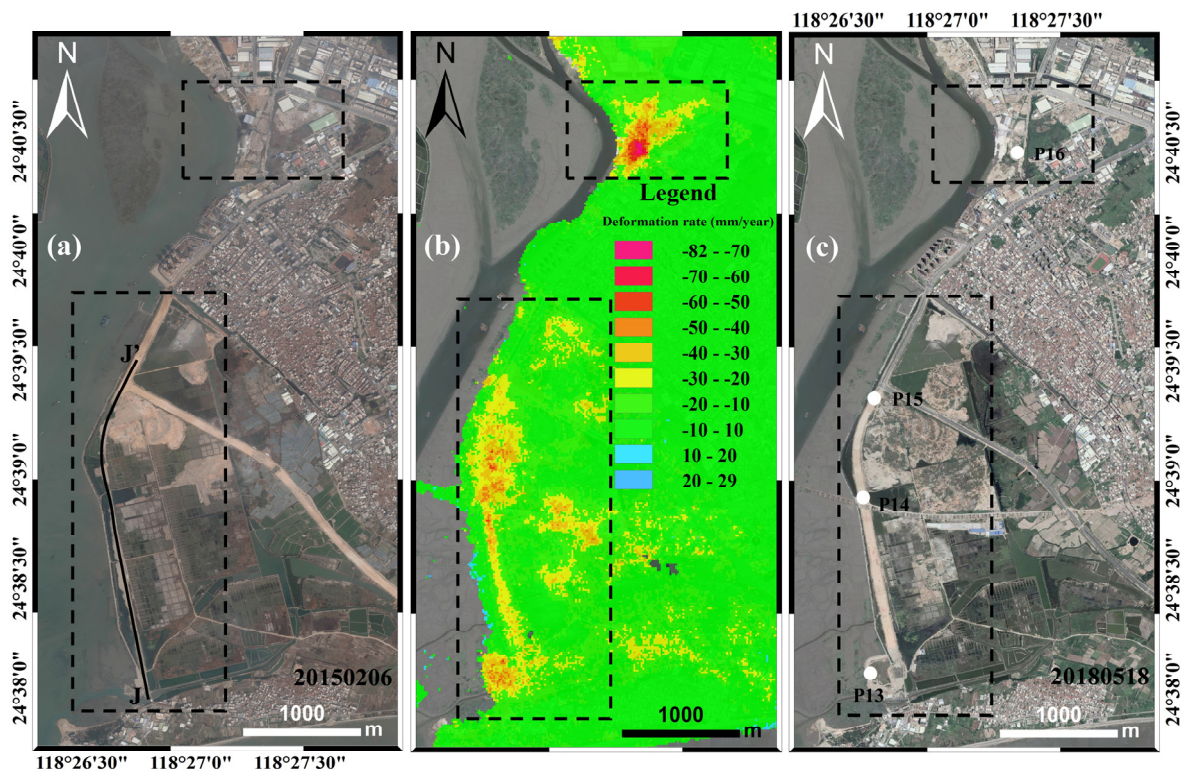


Figure 12. Ground deformation rate and remote sensing images of Region G. (a) Remote sensing image acquired on 6 February 2015; (b) average deformation rate map in the LOS direction from January 2017 to October 2018; (c) remote sensing image acquired on 18 May 2018.

The deformation rate along the road indicated by J–J' (whose position is shown in Figure 12a) was extracted, and it is shown in Figure 13. It can be seen that obvious nonuniform deformation occurred along the newly built road. Deformation in the middle part of the road is greater than that at either end, and several subsidence funnels were observed in the middle section of the road. The maximum deformation rate in the vertical direction reached −57 mm/year. In order to further investigate the temporal evolution of deformation after road construction, three typical points for P13 to P15, located at the two ends and the middle section of the road, were selected to show time series deformation. The locations of the selected points are shown in Figure 12c, and time series deformation is shown in Figure 14. We can see from Figure 14 that the road experienced continuous deformation from January 2017 to October 2018. Maximum cumulative subsidence occurred in the middle section of the road, which reached −125 mm in the vertical direction in less than two years. In addition, it can be found that there were obvious fluctuations in road deformation during the InSAR monitoring period. There is a strong possibility that the results of the InSAR measurement were affected by road construction, as can be seen from the remote sensing images (see Figure 12a,c), since the road was still under construction during the InSAR monitoring period. To verify our speculation, P16 (see Figure 12c) was selected to obtain time series deformation far away from the road construction area, as shown in Figure 14d. It is evident that the time series deformation of P16 did not show obvious fluctuation.

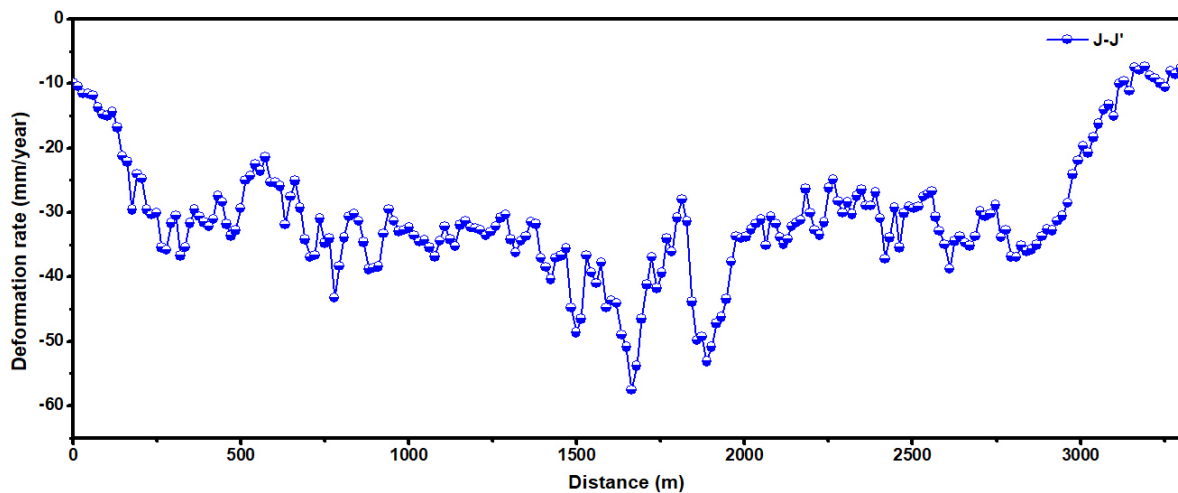


Figure 13. Average deformation rate in the vertical direction of Region G from January 2017 and October 2018 along Profile J-J', whose position are indicated as solid black lines in Figure 12.

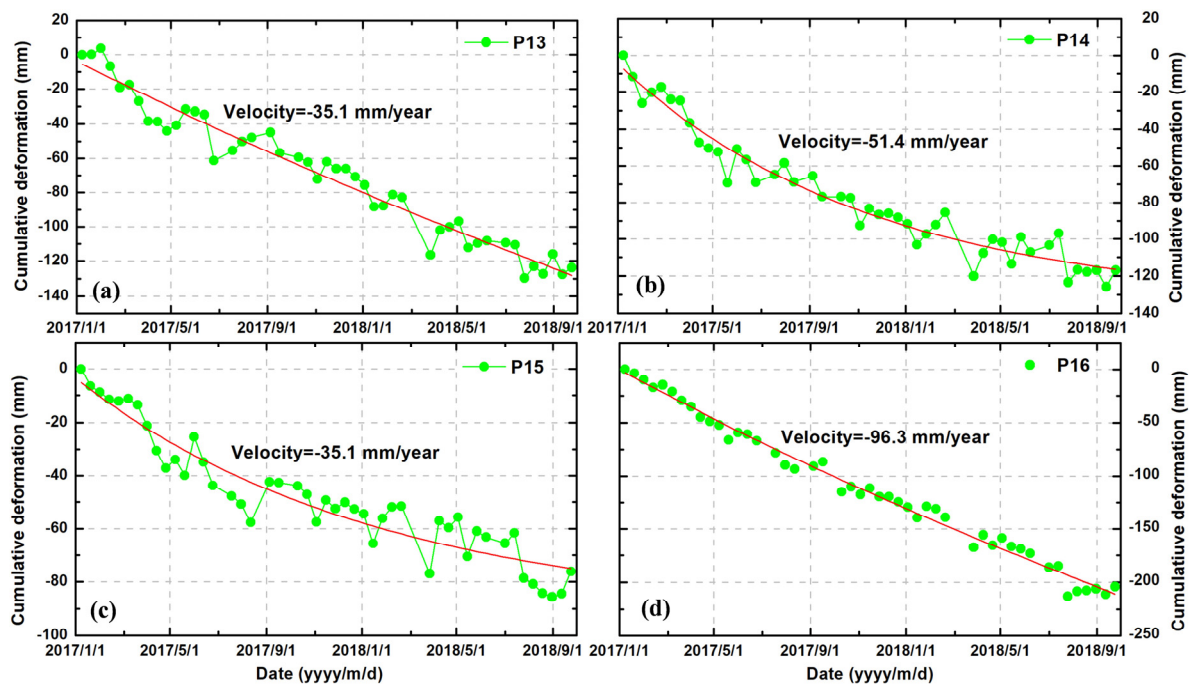


Figure 14. Time series deformation in the vertical direction of Region G from January 2017 and October 2018 for P13 to P16, which are indicated as white dots in Figure 12c. (a) Point P13; (b) point P14; (c) point P15; (d) point 16.

5.5. Detailed Analysis of Land Subsidence at Xiamen New Airport

According to previous investigations [7,10,16,36,37], land subsidence associated with land reclamation is principally induced by three mechanisms: primary consolidation, long-term second compression of alluvial clay deposits beneath the reclamation, and creep with the reclamation fill. The magnitude and velocity of land subsidence after land reclamation largely depends on the types and thickness of the reclaimed materials, the thickness of the underlying alluvial deposits, duration after completion of the reclamation, and the effect of foundation treatment [10,38]. The largest proportion of total subsidence is owed to the primary consolidation of the alluvial clays. In the case of airport land reclamation settlement, it usually amounts to 70% or more [10]. In addition, the subsidence process of primary consolidation is much faster than that of secondary compression and filling creep. Such a phenomenon can be explained by the well-known Terzaghi theory of consolidation [36]. A typical

time-settlement prediction curve for both primary consolidation and secondary compression of alluvial clay under the reclamation is shown in Figure 15 [10]. It can be seen that it underwent sharply rapid deformation (i.e., primary consolidation) after reclamation has just been completed; then, deformation slowed down and finally gradually ceased (i.e., secondary compression). The actual deformation pattern observed by InSAR in Xiamen New Airport is similar to such a time-settlement prediction curve of alluvial clay. Therefore, we can infer that early reclaimed land, like P1 in Figure 7a, completed the primary consolidation stage, and is currently suffering long-term compression. It can also be inferred from Figure 7a that P1 was in the primary consolidation stage before 10 March 2018, and it suffered rapid deformation. Then, it changed to the long-term compression stage after 10 March 2018, and it is currently almost stable. However, newly reclaimed areas completed after August 2016 (see Figure 8), like P4, P8, P10, and P11 (see Figures 7 and 11), are currently still in the primary consolidation stage; accordingly, significant ground deformation will continue for some time.

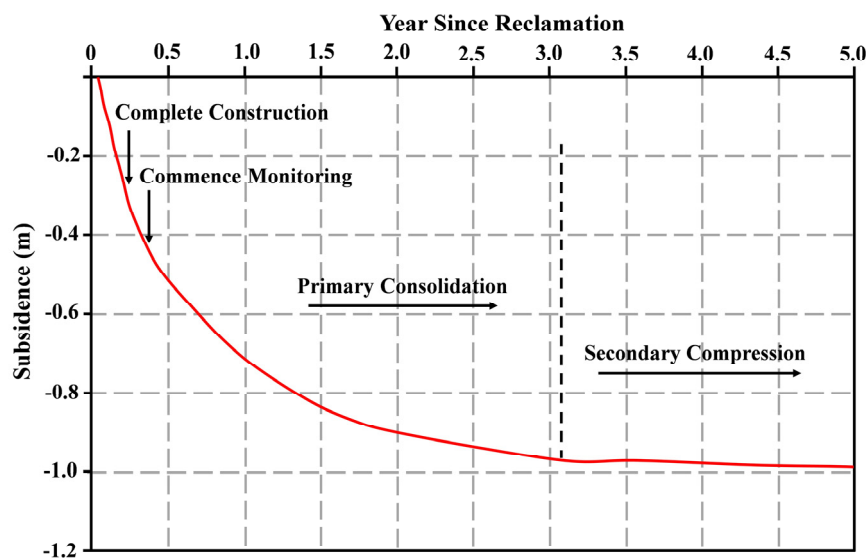


Figure 15. Typical time-settlement prediction curve of alluvial clay under the reclamation, i.e., Terzaghi theory of consolidation [10,36].

6. Conclusions

In this study, the time series InSAR technique was employed to characterize and monitor the ground deformation of Xiamen New Airport after land reclamation. In addition, some land subsidence areas associated with land reclamation were identified in Xiamen's coastal area. A total of 82 ascending Sentinel-1 images were used, which were acquired from August 2015 to October 2018. The pattern and spatiotemporal evolution characteristics of the surface deformation of Xiamen New Airport after land reclamation were fully revealed, providing important deformation information on Xiamen New Airport. The results are of great guiding significance for airport land reclamation, design, and next-stage construction. Furthermore, the airport's deformation characteristic was also successfully validated based on the compression mechanism of the hydraulic fill (i.e., Terzaghi theory of consolidation). The main conclusions that can be drawn are as follows.

A total of 20 land subsidence areas associated with land reclamation were identified in the coastal area of the city of Xiamen from November 2015 to December 2016, which increased to 26 from January 2017 to October 2018. The significant land subsidence areas are mainly concentrated in the central coastal area of Xiamen, i.e., Xiang'an district.

The land subsidence of Xiamen New Airport is mainly concentrated in the area of the second phase of land reclamation. Most reclamation areas underwent a rapid deformation process after completion; then, deformation gradually slowed down and finally became basically stable. Such a

deformation characteristic is similar to the typical time-settlement prediction curve of the alluvial clay under the reclamation, i.e., the Terzaghi theory of consolidation.

Early reclaimed areas are currently in the stage of long-term compression, and deformation is currently small. However, newly reclaimed areas are still in the primary consolidation stage, where rapid deformation is currently underway. In addition, ground surface uplift caused by the rebound of reclamation fill materials after long-term compression was observed in some areas.

Author Contributions: X.L. and C.Z. performed the experiments and produced the results. X.L. drafted the manuscript and C.Z. finalized the manuscript. Q.Z., C.Y., and J.Z. contributed to the discussion of the results. All authors conceived the study, and reviewed and approved the manuscript.

Funding: This research was funded by the Natural Science Foundation of China (Grants No. 41874005, 41731066) and the Fundamental Research Funds for the Central Universities (Grants No. 300102269712).

Acknowledgments: The Sentinel-1A data used in this study were freely provided by Copernicus and ESA, and the one-arc-second SRTM DEM data were freely downloaded from the website http://e4ftl01.cr.usgs.gov/MODV6_Dal_D/SRTM/SRTMGL1.003/2000.02.11/. We thank the three anonymous reviewers as well as the editor for their helpful comments and suggestions.

Conflicts of Interest: The authors declare no conflict of interest.

References

1. Wali, M.K. *Practices and Problems of Land Reclamation in Western North America*; University of North Dakota Press: Grand Forks, ND, USA, 1975.
2. Douglas, I.; Lawson, N. Airport construction: Materials use and geomorphic change. *J. Air Trans. Manag.* **2003**, *9*, 177–185. [[CrossRef](#)]
3. De Mulder, E.; Van Bruchem, A.; Claessen, F.; Hannink, G.; Hulsbergen, J.; Satijn, H. Environmental impact assessment on land reclamation projects in the Netherlands: A case history. *Eng. Geol.* **1994**, *37*, 15–23. [[CrossRef](#)]
4. Suzuki, T. Economic and geographic backgrounds of land reclamation in Japanese ports. *Mar. Pollut. Bull.* **2003**, *47*, 226–229. [[CrossRef](#)]
5. Zhao, Q.; Pepe, A.; Gao, W.; Lu, Z.; Bonano, M.; He, M.L.; Wang, J.; Tang, X. A DInSAR Investigation of the Ground settlement Time Evolution of Ocean-Reclaimed Lands in Shanghai. *IEEE Sel. Top. Appl. Earth Obs. Remote Sens.* **2015**, *8*, 1763–1781. [[CrossRef](#)]
6. Breber, P.; Povilanskas, R.; Armaitiene, A. Recent evolution of fishery and land reclamation in curonian and lesina lagoons. *Hydrobiologia* **2008**, *611*, 105–114. [[CrossRef](#)]
7. Yang, M.S.; Yang, T.L.; Zhang, L.; Lin, J.X.; Qin, X.Q.; Liao, M.S. Spatial-Temporal Characterization of a Reclamation Settlement in the Shanghai Coastal Area with Time Series Analyses of X-, C-, and L-band SAR datasets. *Remote Sens.* **2018**, *10*, 329. [[CrossRef](#)]
8. Pepe, A.; Bonano, M.; Zhao, Q.; Yang, T.L.; Wang, H.M. The Use of C-/X-Band Time-Gapped SAR data and Geotechnical Models for the Study of Shanghai's Ocean-Reclaimed Lands through the SBAS-DInSAR Technique. *Remote Sens.* **2016**, *8*, 911. [[CrossRef](#)]
9. Baek, W.K.; Jung, H.S.; Jo, M.J.; Lee, W.J.; Zhang, L. Ground settlement observation of solid waste landfill park using multi-temporal radar interferometry. *Int. J. Urban Sci.* **2018**, 1–16. [[CrossRef](#)]
10. Jiang, L.M.; Lin, H. Integrated analysis of SAR interferometric and geological data for investigating long-term reclamation settlement of Chek lap KoK Airport, Hong Kong. *Eng. Geol.* **2010**, *110*, 77–92. [[CrossRef](#)]
11. Yu, L.; Yang, T.L.; Zhao, Q.; Liu, M.; Pepe, A. The 2016–2016 ground displacements of the Shanghai coastal area inferred a combined COSMO-SkyMed/Sentinel-1 DInSAR analysis. *Remote Sens.* **2017**, *9*, 1194. [[CrossRef](#)]
12. Liu, P.; Chen, X.F.; Li, Z.H.; Zhang, Z.G.; Xu, J.K.; Feng, W.P.; Wang, C.S.; Hu, Z.W.; Tu, W.; Li, H.Z. Resolving surface displacements in Shenzhen of China from time series InSAR. *Remote Sens.* **2018**, *10*, 1162. [[CrossRef](#)]
13. Aslan, G.; Cakir, Z.; Ergintav, S.; Lassere, G.; Renard, R. Analysis of secular ground motions in Istanbul from a long-term InSAR time series (1992–2017). *Remote Sens.* **2018**, *10*, 408. [[CrossRef](#)]
14. Zebker, H.A.; Villasenor, J. Decorrelation in interferometric radar echoes. *IEEE Trans. Geosci. Remote Sens.* **1992**, *30*, 950–959. [[CrossRef](#)]

15. Yague-Martinez, N.; Prats-Iraola, P.; Gonzalez, F.R.; Brcic, R.; Shau, R.; Geudtner, D.; Eineder, M.; Bamler, R. Interferometric Processing of Sentinel-1 TOPS Data. *IEEE Trans. Geosci. Remote Sens.* **2016**, *54*, 2220–2234. [[CrossRef](#)]
16. Xu, B.; Feng, G.C.; Li, Z.W.; Wang, Q.J.; Wang, C.C.; Xie, R.G. Coastal subsidence monitoring associated with land reclamation using the point target based on SBAS-InSAR method: A case study of Shenzhen, China. *Remote Sens.* **2016**, *8*, 652. [[CrossRef](#)]
17. Berardino, P.; Fornaro, G.; Lanari, R.; Sansosti, E. A new algorithm for surface deformation monitoring based on small baseline differential SAR interferograms. *IEEE Trans. Geosci. Remote Sens.* **2002**, *40*, 2375–2383. [[CrossRef](#)]
18. Mora, O.; Mallorquí, J.J.; Broquetas, A. Linear and nonlinear terrain deformation maps from a reduced set of interferometric SAR images. *IEEE Trans. Geosci. Remote Sens.* **2003**, *41*, 2243–2253. [[CrossRef](#)]
19. Usai, S. A least squares database approach for SAR interferometric data. *IEEE Trans. Geosci. Remote Sens.* **2003**, *41*, 753–760. [[CrossRef](#)]
20. Ferretti, A.; Prati, C.; Rocca, F. Permanent scatterers in SAR interferometry. *IEEE Trans. Geosci. Remote Sens.* **2001**, *39*, 8–20. [[CrossRef](#)]
21. Kampes, B.M. *Radar Interferometry: Persistent Scatterer Technique*; Springer: New York, NY, USA, 2006.
22. Hooper, A.; Zebker, H.; Segall, P.; Kampes, B. A new method for measuring deformation on volcanoes and other natural terrains using InSAR persistent scatterers. *Geophys. Res. Lett.* **2004**, *31*, L23611. [[CrossRef](#)]
23. Xiang'an, Xiamen City, International Airport. Available online: <https://baike.baidu.com/item/%E5%8E%A6%E9%97%A8%E7%BF%94%E5%AE%89%E5%9B%BD%E9%99%85%E6%9C%BA%E5%9C%BA/3898600?fr=aladdin> (accessed on 16 November 2018).
24. Werner, C.; Wegmüller, U.; Strozzi, T.; Wiesmann, A. GAMMA SAR and interferometric processing software. In Proceedings of the ERS-Envisat Symposium, Gothenburg, Sweden, 16–20 October 2000.
25. Sowter, A.; Moh, B.C.A.; Cigna, F.; Marsh, S.; Athab, A.; Alshammari, L. Mexico City land subsidence in 2014–2015 with Sentinel-1 IW TOPS: Results using the Intermittent SBAS (ISBAS) technique. *Int. J. Appl. Earth Obs. Geoinf.* **2016**, *52*, 230–242. [[CrossRef](#)]
26. Scheiber, R.; Moreira, A. Coregistration of interferometric SAR images using spectral diversity. *IEEE Trans. Geosci. Remote Sens.* **2000**, *38*, 2179–2191. [[CrossRef](#)]
27. Jiang, M.; Ding, X.; Hanssen, R.F.; Malhotra, R.; Chang, L. Fast Statistically Homogeneous Pixel Selection for Covariance Matrix Estimation for Multitemporal InSAR. *IEEE Trans. Geosci. Remote Sens.* **2015**, *53*, 1213–1224. [[CrossRef](#)]
28. Jiang, M.; Miao, Z.; Gamba, P.; Yong, B. Application of Multitemporal InSAR Covariance and Information Fusion to Robust Road Extraction. *IEEE Trans. Geosci. Remote Sens.* **2017**, *55*, 3611–3622. [[CrossRef](#)]
29. Goldstein, R.; Werner, C. Radar interferogram filtering for geophysical applications. *Geophys. Res. Lett.* **1998**, *21*, 4035–4038. [[CrossRef](#)]
30. Liu, Y.Y.; Zhao, C.Y.; Zhang, Q.; Yang, C.S. Complex surface deformation monitoring and mechanism inversion over Qingxu-Jiaocheng, China with multi-sensor SAR images. *J. Geodyn.* **2018**, *114*, 41–52. [[CrossRef](#)]
31. Costantini, M. A novel phase unwrapping method based on network programming. *IEEE Trans. Geosci. Remote Sens.* **1998**, *36*, 813–821. [[CrossRef](#)]
32. Kang, Y.; Zhao, C.Y.; Zhang, Q.; Lu, Z.; Li, B. Application of InSAR Techniques to an analysis of the Guanling Landslide. *Remote Sens.* **2017**, *9*, 1046. [[CrossRef](#)]
33. Liu, X.J.; Zhao, C.Y.; Zhang, Q.; Peng, J.B.; Zhu, W.; Lu, Z. Multi-Temporal Loess Landslide Inventory Mapping with C-, X- and L-Band SAR Datasets—A Case Study of Heifangtai Loess Landslides, China. *Remote Sens.* **2018**, *10*, 1756. [[CrossRef](#)]
34. Liao, M.S.; Wang, T. *Time Series InSAR Technique and Application*; Science Press: Beijing, China, 2014; pp. 69–71. (In Chinese)
35. Wang, H.; Wright, T.J.; Yu, Y.; Lin, H.; Jiang, L.; Li, C.; Qiu, G. InSAR reveals coastal subsidence in the Pearl River Delta. *China Geophys. J. Int.* **2012**, *191*, 1119–1128.
36. Terzaghi, K.; Peck, R.B.; Mesri, G. *Soil Mechanics in Engineering Practice*; John Wiley and Sons: Hoboken, NJ, USA, 1996; pp. 1–592.

37. Plant, G.W.; Covil, C.S.; Hughes, R.A. *Site Preparation for the New Hong Kong International Airport—The Design, Construction and Performance of the Airport Platform*; Thomas Telford: London, UK, 1998.
38. Pickles, A.R.; Tosen, R. Settlement of reclaimed land for the new Hong Kong International Airport. *Proc. ICE Geotech. Eng.* **1998**, *131*, 191–209. [[CrossRef](#)]



© 2019 by the authors. Licensee MDPI, Basel, Switzerland. This article is an open access article distributed under the terms and conditions of the Creative Commons Attribution (CC BY) license (<http://creativecommons.org/licenses/by/4.0/>).